THE UNIVERSITY OF ARIZONA
University Libraries

UA CAMPUS REPOSITORY

# HAT-P-67b: An Extremely Low Density Saturn Transiting an F-subgiant Confirmed via Doppler Tomography



| | |
|---|---|
| Item Type | Article |
| Authors | Zhou, G.; Bakos, G. Á.; Hartman, J. D.; Latham, David W.; Torres, G.; Bhatti, W.; Penev, K.; Buchhave, Lars A.; Kovács, G.; Bieryla, A.; Quinn, S.; Isaacson, Howard T.; Fulton, B. J.; Falco, E.; Csubry, Z.; Everett, Mark; Szklenar, T.; Esquerdo, G.; Berlind, P.; Calkins, M. L.; Béky, B.; Knox, R. P.; Hinz, P.; Horch, Elliott; Hirsch, Lea; Howell, Steve B.; Noyes, R. W.; Marcy, G.; Val-Borro, M. de; Lázár, J.; Papp, I.; Sári, P. |
| Citation | HAT-P-67b: An Extremely Low Density Saturn Transiting an F-subgiant Confirmed via Doppler Tomography 2017, 153 (5):211 The Astronomical Journal |
| DOI | 10.3847/1538-3881/aa674a |
| Publisher | IOP PUBLISHING LTD |
| Journal | The Astronomical Journal |
| Rights | © 2017. The American Astronomical Society. All rights reserved. |
| Download date | 27/08/2022 11:34:02 |
| Item License | http://rightsstatements.org/vocab/InC/1.0/ |
| Version | Final published version |
| Link to Item | http://hdl.handle.net/10150/623926 |

The Astronomical Journal, 153:211 (13pp), 2017 May https://doi.org/10.3847/1538-3881/aa674a
© 2017. The American Astronomical Society. All rights reserved.

# HAT-P-67b: An Extremely Low Density Saturn Transiting an F-subgiant Confirmed via Doppler Tomography*

G. Zhou[1], G. Á. Bakos[2,13], J. D. Hartman[2], D. W. Latham[1], G. Torres[1], W. Bhatti[2], K. Penev[2], L. Buchhave[3], G. Kovács[4], A. Bieryla[1], S. Quinn[1], H. Isaacson[5], B. J. Fulton[6], E. Falco[1], Z. Csubry[2], M. Everett[7], T. Szklenar[8], G. Esquerdo[1], P. Berlind[1], M. L. Calkins[1], B. Béky[12], R. P. Knox[9], P. Hinz[9], E. P. Horch[10], L. Hirsch[5], S. B. Howell[11], R. W. Noyes[1], G. Marcy[5], M. de Val-Borro[2], J. Lázár[8], I. Papp[8], and P. Sári[8]

[1] Harvard-Smithsonian Center for Astrophysics, Cambridge, MA 02138, USA
[2] Department of Astrophysical Sciences, Princeton University, Princeton, NJ 08544, USA
[3] Centre for Star and Planet Formation, Natural History Museum of Denmark, University of Copenhagen, DK-1350 Copenhagen, Denmark
[4] Konkoly Observatory of the Hungarian Academy of Sciences, Budapest, Hungary
[5] Department of Astronomy, University of California, Berkeley, CA 94720, USA
[6] Institute for Astronomy, University of Hawaii, Honolulu, HI 96822, USA
[7] National Optical Astronomy Observatory, Tucson, AZ 85719, USA
[8] Hungarian Astronomical Association, Budapest, Hungary
[9] Steward Observatory, University of Arizona, 933 North Cherry Avenue, Tucson, AZ 85721, USA
[10] Department of Physics, Southern Connecticut State University, 501 Crescent Street, New Haven, CT 06515, USA
[11] NASA Ames Research Center, Moffett Field, CA 94035, USA
*Received 2017 January 31; revised 2017 February 19; accepted 2017 March 2; published 2017 April 14*

## Abstract

We report the discovery of HAT-P-67b, which is a hot-Saturn transiting a rapidly rotating F-subgiant. HAT-P-67b has a radius of $R_p = 2.085^{+0.096}_{-0.071}\,R_J$, and orbites a $M_* = 1.642^{+0.155}_{-0.072}\,M_\odot$, $R_* = 2.546^{+0.099}_{-0.084}\,R_\odot$ host star in a ~4.81 day period orbit. We place an upper limit on the mass of the planet via radial velocity measurements to be $M_p < 0.59\,M_J$, and a lower limit of $>0.056\,M_J$ by limitations on Roche lobe overflow. Despite being a subgiant, the host star still exhibits relatively rapid rotation, with a projected rotational velocity of $v \sin I_\star = 35.8 \pm 1.1$ km s$^{-1}$, which makes it difficult to precisely determine the mass of the planet using radial velocities. We validated HAT-P-67b via two Doppler tomographic detections of the planetary transit, which eliminate potential eclipsing binary blend scenarios. The Doppler tomographic observations also confirm that HAT-P-67b has an orbit that is aligned to within 12°, in projection, with the spin of its host star. HAT-P-67b receives strong UV irradiation and is among one of the lowest density planets known, which makes it a good candidate for future UV transit observations in the search for an extended hydrogen exosphere.

*Key words:* planetary systems – stars: individual (HAT-P-67) – techniques: photometric – techniques: spectroscopic

*Supporting material:* machine-readable table

## 1. Introduction

Finding well-characterized planets in a variety of environments is key to understanding the processes that govern planet formation and evolution. Planets orbiting high mass stars are most likely born in high mass protoplanetary disks (e.g., Muzerolle et al. 2003; Natta et al. 2006), which are environments that may yield higher planet occurrence rates (e.g., Johnson et al. 2010; Bowler et al. 2010) and higher mass planets (e.g., Jones et al. 2014; Lovis & Mayor 2007) than those around solar-type stars. Planets around early-type stars also receive a higher incident flux over their lifetimes, which in turn make them anchor-points in the planet mass–radius-equilibrium temperature relationships (e.g., Béky et al. 2011; Enoch et al. 2012).

However, only 1% of known transiting planets orbit stars that are more massive than 1.5 $M_\odot$. Early-type stars have larger radii, which result in shallower transit depths for any planets; they are also more likely to have rotationally-blended spectral lines due to the lack of magnetic braking over the main-sequence lifetime, which makes traditional radial velocity confirmation techniques more difficult. One successful strategy is to conduct radial velocity surveys of "retired A-stars" (i.e., stars that have evolved off the main sequence and have spun down enough to exhibit sharp spectroscopic lines that enable precise radial velocity measurements). These surveys have been extremely successful and have yielded 122 planetary systems to date[14] (e.g., Johnson et al. 2007; Wittenmyer et al. 2011; Jones et al. 2014). Recently, transit surveys have successfully discovered planets around high mass stars. These

* Based on observations obtained with the Hungarian-made Automated Telescope Network. Based in part on observations made with the Keck-I telescope at Mauna Kea Observatory, HI (Keck time awarded through NASA programs N029Hr, N108Hr, N154Hr, and N130Hr; and NOAO programs A289Hr and A284Hr). Based in part on observations obtained with the Tillinghast Reflector 1.5 m telescope and the 1.2 m telescope, both of which are operated by the Smithsonian Astrophysical Observatory at the Fred Lawrence Whipple Observatory in Arizona. This work makes use of the Smithsonian Institution High Performance Cluster (SI/HPC). Based in part on observations made with the Nordic Optical Telescope, operated on the island of La Palma jointly by Denmark, Finland, Iceland, Norway, and Sweden, in the Spanish Observatorio del Roque de los Muchachos of the Instituto de Astrofísica de Canarias.

[12] Google Inc.

[13] Packard Fellow.

[14] Choosing host stars with $\log g < 4.0$ from the NASA Exoplanet Archive, 2016 July.

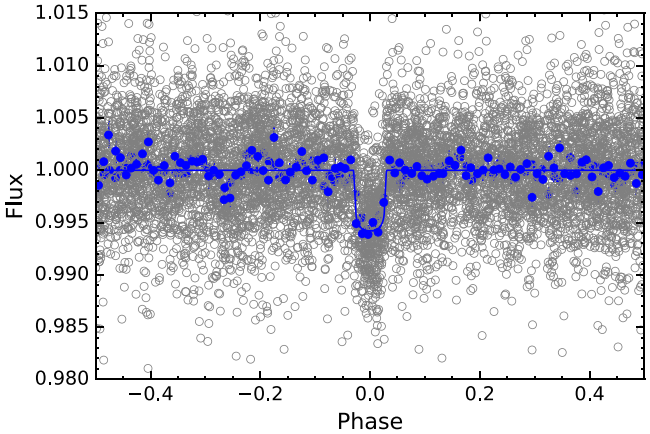


**Figure 1.** HATNet discovery light curves showing the transit of HAT-P-67b. The light curve is phase folded to a period of $P = 4.8101050$ days, as per the analysis in Section 3. Gray points show the raw light curve, while blue points show the data binned at 0.01 in the phase. The solid blue line shows the best-fit transit model from Section 3.4.

include planets around subgiants and giants whose shallow transits were identified by *Kepler* (e.g., Kepler-56b,c, Huber et al. 2013; Kepler-91b, Lillo-Box et al. 2014; Kepler-432b, Ciceri et al. 2015, Quinn et al. 2015; KOI-206b and KOI-680b, Almenara et al. 2015; and K2-39b, Van Eylen et al. 2016) and hot-Jupiters around main-sequence A-stars confirmed via Doppler tomography (WASP-33b, Collier Cameron et al. 2010b; Kepler-13b, Shporer et al. 2011, Szabó et al. 2011, Johnson et al. 2014; HAT-P-57b, Hartman et al. 2015; and KELT-17b, Zhou et al. 2016b).

In this paper, we present the discovery of HAT-P-67b, which is a Saturn-mass planet that was found to transit an F-subgiant by the HATNet survey (Bakos et al. 2004). Despite the evolved status of HAT-P-67, the host star still exhibits a rapid rotation rate of $v \sin I_\star = 35.8 \pm 1.1$ km s$^{-1}$, which makes precise radial velocities difficult to obtain. Eventual confirmation was achieved via a detection of the Doppler tomographic shadow of the planet during transit. When a planet transits a rapidly rotating star, it successively blocks parts of the rotating stellar disk, therefore causing an asymmetry in the observed spectral line profiles. At low rotational velocities, the asymmetry can be measured by the Holt–Rossiter–McLaughlin effect (Holt 1893; McLaughlin 1924; Rossiter 1924). At higher rotational velocities, the shadow of the planet can be resolved in the broadened stellar spectroscopic lines (e.g., Collier Cameron et al. 2010a, 2010b). A detection of the Doppler tomographic signal, at a depth and width that are in agreement with the photometric transit, eliminates eclipsing binary blend scenarios that may mimic transiting planet signals. Further radial velocity measurements can then provide an upper-limit mass constraint of the orbiting companion. If the mass can be constrained to less than that of brown dwarfs, then the transiting object is confirmed to be a planet.

## 2. Observations

### 2.1. Photometry

The transits of HAT-P-67b were first detected with the HATNet survey (Bakos et al. 2004). HATNet employs a network of small, wide field telescopes, located at the Fred Lawrence Whipple Observatory (FLWO) in Arizona and at the Mauna Kea Observatory (MKO) in Hawaii, to photometrically monitor selected $8 \times 8°$ fields of the sky. A total of 4050 $I$ band observations were taken by HAT-5 and HAT-8 from 2005 January to July, and an additional 4518 observations were obtained in the Cousins $R$ band using HAT-5, HAT-7, and HAT-8 telescopes between 2008 February and August. The data reduction follows Bakos et al. (2010). Light curves were produced via aperture photometry and detrended with External Parameter Decorrelation (EPD, Bakos et al. 2007) and Trend Filtering Algorithm (TFA, Kovács et al. 2005). The Box-fitting Least Squares (Kovács et al. 2002) analysis revealed the periodic transits of the planet candidate. The discovery light curve of HAT-P-67b is shown in Figure 1, and the photometry is presented in Table 1.

To better characterize the planetary properties, follow-up photometry of the transits were obtained using the KeplerCam on the FWLO 1.2 m telescope. KeplerCam is a 4K × 4 K CCD camera with a pixel scale of $0\farcs672$ pixel$^{-1}$ at $2 \times 2$ pixel binning. The photometry was reduced as per Bakos et al. (2010). A full transit was observed in the Sloan-$i$ band on 2012 May 28, and five partial transits were observed on 2011 April 15, May 19, June 07, and 2013 April 25 in the Sloan-$i$ band, and 2013 May 24 in the Sloan-$z$ band. The light curves and best-fit models are shown in Figure 2, and the data are presented in Table 1. A summary of the photometric observations are presented in Table 2.

### 2.2. Spectroscopy

Spectroscopic observations of HAT-P-67 were carried out using the FIber-fed Echelle Spectrograph (FIES), the Tillinghast Reflector Echelle Spectrograph (TRES), and the High Resolution Echelle Spectrometer (HIRES).

An initial spectroscopic characterization of HAT-P-67b was obtained with the FIES instrument (Telting et al. 2014) on the 2.5 m Nordic Optical Telescope (NOT). FIES is a fiber-fed, high-resolution echelle spectrograph with a resolution of $\lambda/\Delta\lambda \equiv R = 67{,}000$ and a spectral coverage of 3700–7300 Å. Four FIES radial velocities were obtained over the 2009 August to October period. The observations were obtained and reduced as per the procedure from Buchhave et al. (2010). Radial velocity variation was not detected by the FIES observations, with a scatter of 200 m s$^{-1}$ over the four observations.

Additional observations were obtained with the TRES instrument (Fűrész 2008) on the FLWO 1.5 m telescope. TRES is a fiber-fed echelle with a spectral resolution of $R = 44{,}000$ over the spectral region of 3850–9100 Å. Radial velocities and spectral classifications are measured from each spectrum as per Buchhave et al. (2012). Each TRES observation consists of three exposures combined together for cosmic-ray removal, and are wavelength calibrated by Th-Ar lamp exposures, which bracket each set of three exposures. Two TRES observations at phase quadrature were taken on 2011 April 17 and April 20, with the signal to noise at the Mg b lines of ∼100 per resolution element. The velocity difference between the two observations was 80 m s$^{-1}$, with a per-point uncertainty of 100 m s$^{-1}$. As such, the the FIES and TRES observations showed that any companion orbiting HAT-P-67 must be a subbrown dwarf in mass.

In addition, we observed two partial spectroscopic transits of HAT-P-67b, on 2016 April 17 and May 16 and using TRES to detect the Doppler tomographic shadow of the planet. These observations were performed as per the strategy described in

**Table 1**
Differential Photometry of HAT-P-67

| BJD | Mag (Raw) | Mag (EPD) | Mag (TFA) | $\sigma$ Mag | Instrument | Filter |
|---|---|---|---|---|---|---|
| 2454521.99042 | 9.39859 | 9.72414 | 9.72271 | 0.00303 | HATNet | R |
| 2454521.99445 | 9.39572 | 9.72048 | 9.73067 | 0.00325 | HATNet | R |
| 2454521.99854 | 9.39262 | 9.72005 | 9.71695 | 0.00276 | HATNet | R |
| 2454522.00264 | 9.38941 | 9.7199 | 9.72327 | 0.00344 | HATNet | R |
| 2454522.00673 | 9.41475 | 9.74011 | 9.73327 | 0.00328 | HATNet | R |

**Note.** Raw, EPD, and TFA magnitudes are presented for HATNet light curves. The detrending and potential blending may cause the HATNet transit to be shallower than the true transit in the EPD and TFA light curves. This is accounted for in the global modeling by the inclusion of a third light factor. Follow-up light curves have been treated with the EPD simultaneous to the transit fitting. Pre-EPD magnitudes are presented for the follow-up light curves.

(This table is available in its entirety in machine-readable form.)

**Table 2**
Summary of Photometric Observations

| Facility | Date(s) | Number of Images[a] | Cadence (s)[b] | Filter |
|---|---|---|---|---|
| HATNet | 2005 Jan–Jul | 4050 | 328 | *I* |
| HATNet | 2008 Feb–Aug | 4518 | 246 | Cousins *R* |
| FLWO 1.2 m KeplerCam | 2011 Apr 15 | 730 | 24 | Sloan-*i* |
| FLWO 1.2 m KeplerCam | 2011 May 19 | 509 | 44 | Sloan-*i* |
| FLWO 1.2 m KeplerCam | 2011 Jun 07 | 801 | 29 | Sloan-*i* |
| FLWO 1.2 m KeplerCam | 2012 May 28 | 730 | 34 | Sloan-*i* |
| FLWO 1.2 m KeplerCam | 2013 Apr 25 | 960 | 24 | Sloan-*i* |
| FLWO 1.2 m KeplerCam | 2013 May 24 | 361 | 24 | Sloan-*z* |

**Notes.**
[a] Outlying exposures have been discarded.
[b] Median time difference between points in the light curve. Uniform sampling was not possible due to visibility, weather, and pauses.

Zhou et al. (2016a). A set of time series spectra, at 900 s cadence, were collected on both nights. The Doppler tomographic analysis for these two transit sets are described in Section 3.1.

To constrain the mass of the companion, we obtain spectroscopic observations from HIRES on the 10 m KECK telescope (Vogt et al. 1994) at MKO over the 2009 July to 2012 March period. A total of 19 observations were obtained through the $I_2$ cell, which provided precise radial velocities. An additional $I_2$-free observation was obtained to provide a template for the radial velocity measurements. The instrument was set up to use the C2 decker, which provides a $14'' \times 0\farcs861$ slit and yields a spectral resolution of $R = 48{,}000$. The radial velocities were measured as per Butler et al. (1996), and the bisector spans (BS) were calculated as per Torres et al. (2007). The high signal-to-noise HIRES observations provide the best constraints on the radial velocities of HAT-P-67 and were used in the global analysis in Section 3.4. The radial velocities from HIRES are plotted in Figure 3 and are presented in Table 3. A summary of the spectroscopic observations are presented in Table 4.

## 3. Analysis

### 3.1. Doppler Tomographic Detection of the Planetary Transit

The significant rotational broadening of HAT-P-67 allows us to detect the spectroscopic transit of the planet via the Doppler tomography (Collier Cameron et al. 2010a, 2010b). Two sets of transit spectroscopy were obtained for HAT-P-67b with TRES. The TRES spectra were processed as per the procedure laid out in Zhou et al. (2016a): the broadening profiles were derived via a least-squares deconvolution (LSD) of the observed spectra against a nonrotating stellar template (as per Donati et al. 1997). Synthetic template spectra were generated using the SPECTRUM (Gray & Corbally 1994) spectral synthesis program, which used the ATLAS9 model atmospheres (Castelli & Kurucz 2004). The synthetic templates were generated at the same $T_{\rm eff}$, $\log g$, and [Fe/H] as HAT-P-67, without line broadening being imposed. A broadening profile was derived for each spectrum and subtracted from the average out-of-transit profile, which revealed the planetary transit signal (see Figure 4). We model the rotational profiles and the planetary signal as part of our global analysis, which we describe in Section 3.4.

### 3.2. Stellar Parameters

Stellar atmospheric parameters of HAT-P-67 were derived from the 32 TRES spectra using the Stellar Parameter Classification pipeline (SPC, Buchhave et al. 2012). We first run the SPC to retrieve an initial estimate of the stellar atmospheric parameters. These are then incorporated into a first run of the global modeling and isochrone retrieval analysis described later in Section 3.4. We then re-run the SPC with the stellar surface gravity $\log g$ fixed to that measured from the transit duration in the global analysis (Section 3.4, with $\log g = 3.854^{+0.014}_{-0.023}$) to provide updated and better constrained $T_{\rm eff}$ and [Fe/H] values. We find that HAT-P-67 is consistent with an F-subgiant of the effective temperature $T_{\rm eff} = 6406 \pm 62$ K, metallicity $[{\rm m/H}] = -0.08 \pm 0.05$, and projected rotational velocity $v \sin I_\star = 36.5 \pm 0.3$ km s$^{-1}$. Similarly, running the SPC on the four FIES spectra yields $T_{\rm eff} = 6380 \pm 50$ K, $\log g = 3.91 \pm 0.10$, $[{\rm m/H}] = -0.05 \pm$

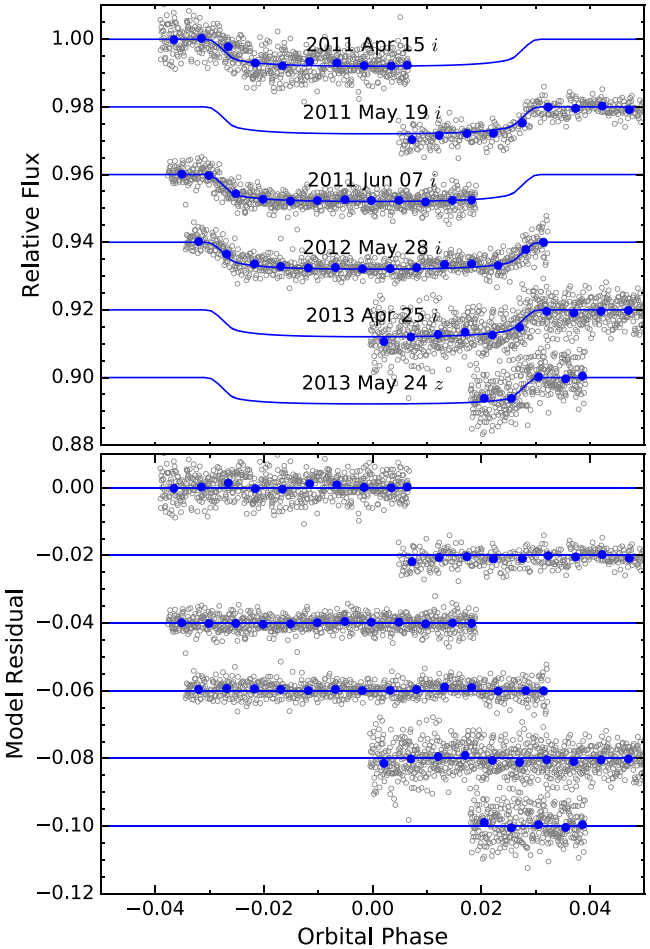


**Figure 2.** Follow-up transit light curves of HAT-P-67b obtained by the KeplerCam on the FLWO 1.2 m telescope. The individual transits are labeled and arbitrarily offset along the $y$ axis for clarity. The raw light curves are plotted in gray and phase binned at 0.005 intervals shown in blue. The best-fit models are plotted in blue. The residuals are shown in the bottom panel.

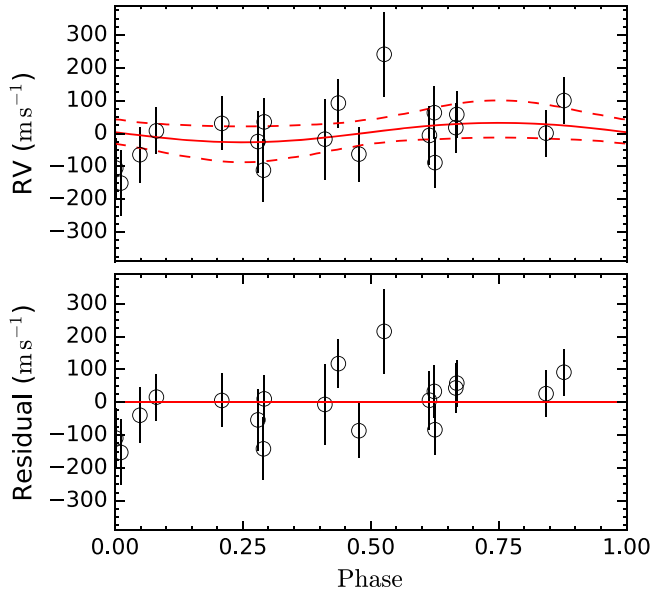


**Figure 3.** Radial velocities from KECK-HIRES for HAT-P-67. The observations are marked by the open circles. The best-fit circular orbit model is shown by the solid red line; the dashed lines encompass the $2\sigma$ set of models allowed by the data. The residuals are plotted in the bottom panel.

**Table 3**
KECK-HIRES Relative Radial Velocities and Bisector Span Measurements of HAT-P-67

| BJD (UTC) | RV[a] (m s$^{-1}$) | $\sigma$ RV (m s$^{-1}$) | BS (m s$^{-1}$) | $\sigma$ BS (m s$^{-1}$) |
|---|---|---|---|---|
| 2455696.8366 | −105 | 28 | 24 | 11 |
| 2455696.88382 | −151 | 31 | 67 | 17 |
| 2455697.833 | 31 | 25 | −58 | 9 |
| 2455698.92918 | 93 | 23 | −53 | 8 |
| 2455699.83162 | 63 | 25 | 46 | 10 |
| 2455700.88206 | 1 | 22 | 30 | 13 |
| 2455704.84352 | 18 | 23 | −2 | 13 |
| 2455705.86007 | 100 | 22 | −34 | 8 |
| 2455706.83882 | 8 | 22 | 14 | 11 |
| 2455707.85238 | 35 | 22 | −17 | 13 |
| 2455853.70871 | −6 | 28 | ... | ... |
| 2455945.15236 | −89 | 24 | ... | ... |
| 2455997.02884 | −17 | 38 | ... | ... |
| 2455017.0082 | 58 | 22 | ... | ... |
| 2455042.88956 | −65 | 26 | ... | ... |
| 2455043.9989 | −25 | 29 | ... | ... |
| 2455044.94822 | −63 | 26 | ... | ... |
| 2455048.86097 | −112 | 30 | ... | ... |
| 2455107.71733 | 241 | 40 | −3 | 28 |

**Note.**
[a] Internal errors, excluding the component of astrophysical/instrumental jitter, are considered in Section 3. BS are given where available.

0.08, and $v \sin I_\star = 38$ km s$^{-1}$, which are consistent with the interpretation that HAT-P-67 is an F-subgiant. Since an accurate $v \sin I_\star$ measurement is vital to correctly model the Doppler tomographic signal, we also use the set of time series TRES spectra to measure the $v \sin I_\star$ of HAT-P-67. Following Zhou et al. (2016a), the broadening kernel for each spectrum is modeled by a rotational kernel, with width of $v \sin I_\star$ and a Gaussian kernel to account for macroturbulence and instrumental broadening, which finds $v \sin I_\star = 30.9 \pm 2.0$ km s$^{-1}$ and a macroturbulence of $9.22 \pm 0.5$ km s$^{-1}$. The uncertainties are estimated from the standard deviation scatter between exposures. The difference between the $v \sin I_\star$ measured via the SPC and that from the rotational profile can be partially attributed to the inclusion of macroturbulence.

### 3.3. GAIA Parallax

HAT-P-67 is included in the *Tycho-GAIA*-Astrometric-Catalogue in the first data release (DR1) of *GAIA* (Lindegren et al. 2016), which measures a parallax of $2.60 \pm 0.23$ mas. Several literature investigations have pointed out a systematic under-estimation in the DR1 parallaxes, as per separate studies via eclipsing binaries (Stassun & Torres 2016), close-by Cepheids (Casertano et al. 2016), asteroseismic distances (Silva Aguirre et al. 2016), and comparisons with existing parallaxes of solar neighborhood stars (Jao et al. 2016). We adopt the correction offered in Stassun & Torres (2016) of $-0.325 \pm 0.062$ mas to the DR1 parallax of HAT-P-67, and arriv at an adopted parallax value of $2.92 \pm 0.23$ mas, and corresponding astrometric distance measurement of $342 \pm 27$ pc. This parallax measurement is used to co-constrain the stellar parameters during the global modeling, which is described in Section 3.4.

**Table 4**
Summary of Spectroscopic Observations

| Telescope/Instrument | Date Range | Number of Observations | Resolution | Observing Mode |
|---|---|---|---|---|
| NOT 2.5 m/FIES | 2009 Aug 4–Oct 10 | 5 | 67,000 | RECON RV |
| FLWO 1.5 m/TRES | 2011 Apr 17–20 | 2 | 44,000 | RECON RV |
| KECK 10 m/HIRES | 2009 Jul 04–2012 Mar 10 | 19 | 55,000 | RV[a] |
| FLWO 1.5 m/TRES | 2016 Apr 17 | 14 | 44,000 | Transit[b] |
| FLWO 1.5 m/TRES | 2016 May 16 | 16 | 44,000 | Transit[b] |

**Notes.**
[a] High resolution spectra to obtain stellar atmospheric parameters and high precision radial velocities.
[b] High resolution in-transit spectra to detect the Doppler tomographic signal of the planet.

### *3.4. Global Fitting and Derived Planet Parameters*

We perform a global analysis of the HATNet discovery light curves, follow-up transit light curves, KECK-HIRES $I_2$ radial velocities, and the TRES Doppler tomographic signal, which is co-constrained by stellar isochrones and the *GAIA* distance measurement. The transits are modeled according to Mandel & Agol (2002), with the transit shape defined by the transit centroid time $T_0$, star–planet distance $a/R_\star$, planet–star radius ratio $R_p/R_\star$, and transit inclination $i$. Individual quadratic limb darkening parameters are assigned to each light curve (interpolated from Claret & Bloemen 2011) and fixed throughout the fitting. Separate dilution factors are allowed for the HATNet $I$ and $R_C$ band light curves to account for any distortions to the light curve shape from the TFA detrending process. The follow-up light curves are simultaneously detrended against instrumental parameters that describe the $X$, $Y$ pixel centroids of the target star, background flux, and target air mass. The radial velocities are described by an arbitrary offset $\gamma$ and orbital semi-amplitude $K$. The orbital eccentricity parameters $e\cos\omega$ and $e\sin\omega$ are also included when eccentricity is allowed to vary. The Doppler tomographic signal is modeled as per Zhou et al. (2016b) via a 2D integration of the stellar surface covered by the planet. The free parameters that describe the Doppler tomography effect include the projected spin–orbit angle $\lambda$ and the projected rotational broadening velocity $v\sin I_\star$. Note that we do not account for the broadening of the planetary shadow due to the motion of the planet during an exposure; the blurring of the planetary shadow during an exposure (2 km s$^{-1}$) is smaller than the width of the shadow (7.2 km s$^{-1}$), but is not an insignificant effect. We also allow the effective temperature $T_{\rm eff}$, metallicity [M/H], and the apparent $K$-band magnitude to be iterated, although heavily constrained, around their spectroscopic and photometric values. At each step, we derive a stellar density $\rho_\star$ from the transit duration as per Seager & Mallén-Ornelas (2003) and Sozzetti et al. (2007), and query the stellar isochrones to derive a distance modulus. Isochrone interpolation is performed at each step using the gradient boosting regression algorithm implemented in *scikit-learn*. This distance modulus is compared to the actual distance as measured from the *0* parallax, with the difference applied as a penalty on the likelihood function.

The rapid rotation rate of HAT-P-67 can introduce a bias in the isochrone-derived parameters for the system. For stars with radiative envelopes, the convective core overshoot and mixing length parameters are different than that of nonrotating stellar models, with the overall effect of lengthening the main-sequence lifetime (e.g., Meynet & Maeder 2000). We adopt the Geneva 2D stellar evolution models (Ekström et al. 2012) for our analysis, which account for the effects of rotation. For the isochrone fitting, we introduce the added dimension of equatorial velocity $v_{\rm eq}$ into our interpolation. The $v_{\rm eq}$ distribution is calculated from the measured $v\sin I_\star$ value, and is scaled by a uniform distribution of orientations sampled in $\cos I_\star$.

To compare our Geneva isochrone results to fittings with more traditional 1D isochrones, we also present the results from analyses using the Dartmouth isochrones (Dotter et al. 2008).

The parameter space is explored with a Markov chain Monte Carlo (MCMC) analysis, which uses the affine-invariant ensemble sampler *emcee* (Foreman-Mackey et al. 2013). The observations are fitted twice, with the per-point uncertainties for each data set inflated to such that the reduced $\chi^2$ is at unity for the second run. A $\cos i$ prior is imposed on the transit inclination, while a Gaussian prior is imposed on $T_{\rm eff} = 6406 \pm 64$ K, $[{\rm M/H}] = 0.08 \pm 0.05$ and $v\sin I_\star = 30.9 \pm 2.0$ km s$^{-1}$ based on the spectroscopic values outlined in Section 3.2. We note that the derived posterior $v\sin I_\star$ ($35.8 \pm 1.1$ km s$^{-1}$) is offset with the prior by $\sim 2\sigma$. Resetting the prior to $35.8 \pm 1.1$ km s$^{-1}$ did not change the system parameters significantly, and resulted ina derived $\lambda$ $1\sigma$ upper limit of $<11°$ (compared to $<14°$ from our adopted results). The $K$-band magnitude is also constrained by a Gaussian prior around its 2MASS value (Skrutskie et al. 2006). The *GAIA* parallax is also heavily constrained by a Gaussian prior around our adopted value of $2.92 \pm 0.23$ mas, as described in Section 3.2. A $\beta$ distribution prior is imposed on the eccentricity, which follows the prescription for short period planets set out by Kipping (2013). Uniform priors are imposed on all other parameters.

Due to the large radius of HAT-P-67b, potential solutions in the MCMC chain lead to the planet overflowing its Roche lobe (e.g., Lecavelier des Etangs et al. 2004). We can use this to place a lower limit on the mass of the planet by assuming that there isn't a Roche lobe overflow. For each link of the MCMC chain, we calculate the corresponding Roche lobe radius using Equation A5 of Hartman et al. (2011). Links with $R_p/a$ overflowing the Roche lobe are eliminated. For the circular orbit fit, the Roche lobe provides a weak lower limit on the mass of the planet of 0.056 $M_{\rm J}$. The posterior distribution for planet mass is plotted in Figure 5. The final mass measurement we report is at the 68% confidence interval for the Roche lobe constrained posterior distribution.

We present four sets of solutions in Tables 5 and 6 for the circular and eccentric orbit scenarios from the Geneva and Dartmouth isochrone fits. The circular orbit Geneva isochrone fit solution is preferred over the eccentric solution with a

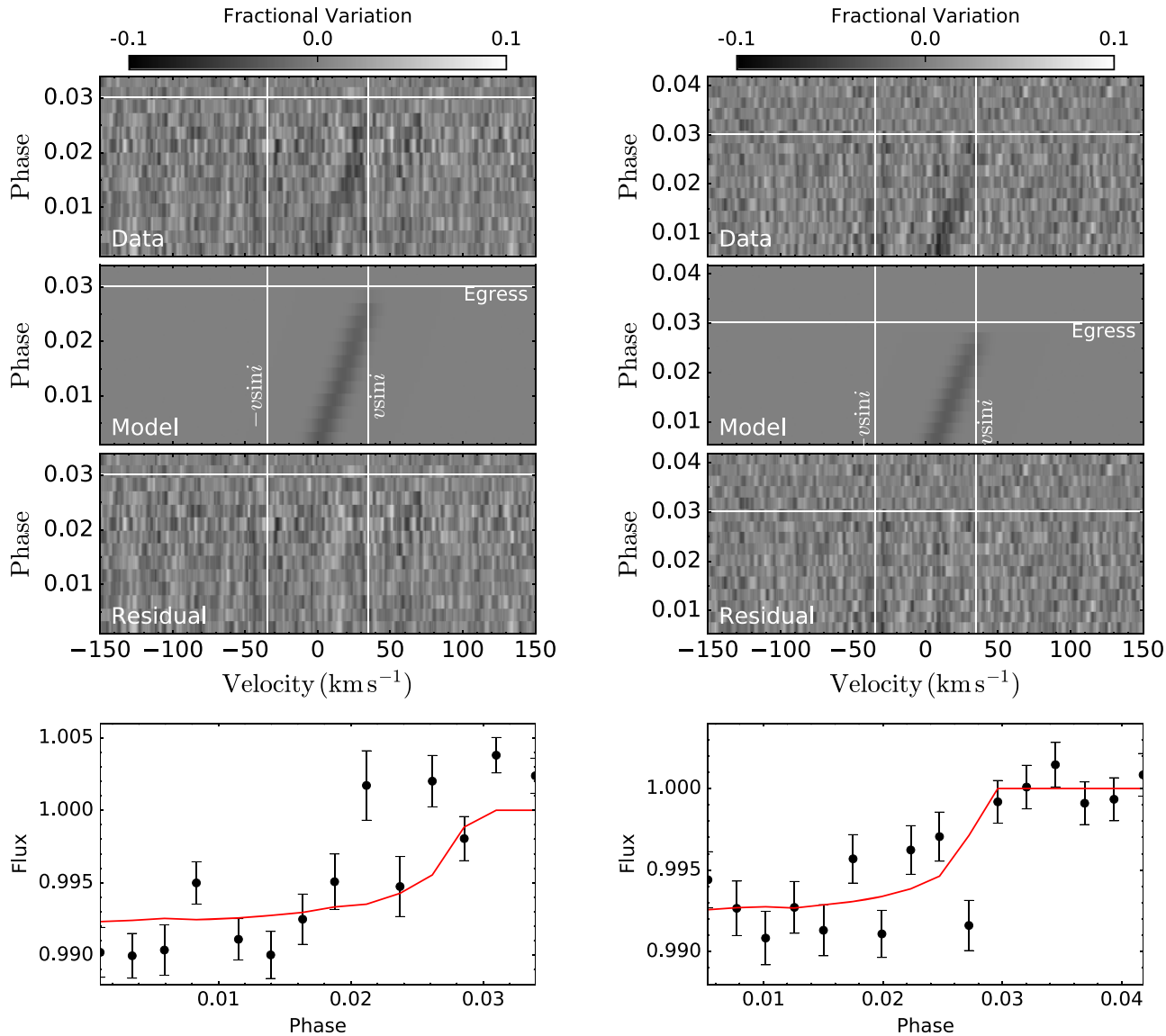


**Figure 4.** Doppler tomographic signals for the spectroscopic transits of HAT-P-67b on 2016 April 17 (left) and 2016 May 16 (right). The top panels show the residual between the broadening kernel from each observation and that of the averaged out-of-transit broadening kernel. The transit can be seen as the dark streak running diagonally from bottom left (mid-transit) to the top right (post-egress). The best-fit models are plotted below, as are the residual after subtraction of the modeled planetary tomographic signal. The bottom panels show the reconstructed light curves from the Doppler tomographic observation. These are constructed by summing the signal under the Doppler tomographic "shadow" of the planet. The red line shows the expected signal from the photometric transit, which is in agreement with the transit depth modeled via the Doppler tomography and eliminates potential blend scenarios for the system.

Bayesian Information Criterion ΔBIC of 212. That is because the increased degrees of freedom in an eccentric orbit fit do not justify the improvements in the goodness of fit over that of a circular orbit model.

The evolutionary stage of HAT-P-67 is shown in Figure 6 on the Hertzsprung-Russell diagram, along with evolutionary tracks of various stellar masses and rotation rates that are marked for context. The derived stellar and planetary parameters are presented in Tables 5 and 6, respectively.

### 3.5. Eccentricity Constraint

We can constrain the eccentricity of the system via the photometric light curves despite a lack of detection of the radial velocity orbit because the *GAIA* parallax provides a good constraint on the stellar radius and transit duration (Kipping 2008; Dawson & Johnson 2012). The eccentricity posterior, as constrained primarily from this "photo-eccentric" effect, is shown in Figure 7. The eccentricity $2\sigma$ upper limit is 0.43, with a posterior median and 64% confidence region of ecc = $0.24 \pm 0.12$.

The parallax we choose to adopt has an effect on our best-fit solutions. If we choose to adopt the *GAIA* parallax of $2.60 \pm 0.23$ mas ($385 \pm 34$pc) from Lindegren et al. (2016) without the systematic correction offered by Stassun & Torres (2016), we would have a modest $1.3\sigma$ tension between the best-fit isochrone distance and the parallax distance. Adopting a distance of $385 \pm 34$ pc yields an eccentric orbit of $e = 0.356^{+0.072}_{-0.077}$. The tidal circularization timescale for the system is $<500$ Myr (Dobbs-Dixon et al. 2004), so the likelihood of such an eccentric orbit is low for the system.

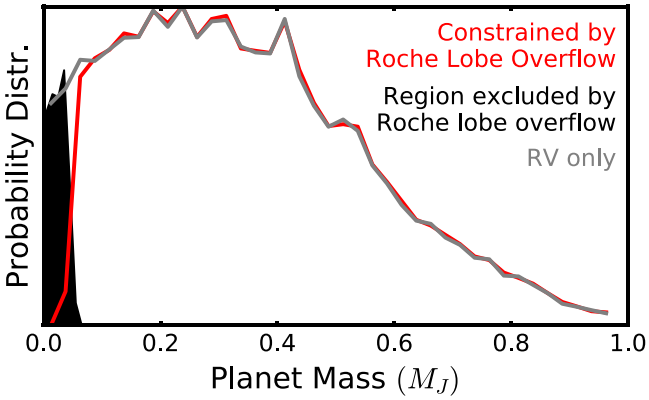


**Figure 5.** Posterior distribution for the mass of the planet. The gray line shows the posterior distribution constrained only by the radial velocities, from which an upper limit of 0.59 $M_J$ can be derived. A lower limit of 0.056 $M_J$ can also be applied if we assume that the planet is not undergoing a Roche lobe overflow. The resulting mass distribution is marked by the red line, while the solutions excluded are filled in black.

### 3.6. Transit Timing Variations and Additional Companions

To check for potential transit timing variations that may be indicative of additional orbiting companions, we refit the follow-up transit observations, which allows for individual transit centroids for each epoch. The timing residuals are shown in Figure 8. The transit geometry parameters $a/R_\star$, $R_p/R_\star$, and inclination are heavily constrained by Gaussian priors around their best-fit values from the global analysis (adopted as the circular orbit fit in Table 6). We do not find convincing evidence for transit timing variations; but we also note that the ~7 hr transit duration makes it difficult for us to capture full transits via a ground-based follow-up, and partial transits provide poorer transit timing measurements. In addition, we do not find evidence for long term radial velocity trend, with the quadratic and linear fits to the radial velocity data consistent with flat slopes.

### 3.7. Imaging Constraints on Resolved Neighbors

In order to detect possible neighboring stars that may be diluting the photometric transits, we obtained optical and near-infrared imaging of HAT-P-67 using the Clio2 near-IR imager (Freed et al. 2004) on the MMT 6.5 m telescope on Mt. Hopkins in Arizona; together with the Differential Speckle Survey Instrument (DSSI; Howell et al. 2011; Horch et al. 2012, 2011); and the WIYN High-Resolution Infrared Camera (WHIRC), both of which are on the WIYN 3.5 m telescope[15] at Kitt Peak National Observatory in Arizona.

The Clio2 images were obtained on the night of UT 2011 June 22. Observations in the $H$-band and $L'$-band were made using the adaptive optics (AO) system. A possible neighbor was detected 4.″9 to the southeast of HAT-P-67 with a relative magnitude difference of $\Delta H = 7.4 \pm 0.5$ mag, but no other closer objects were seen. The neighbor was blended with HAT-P-67 in the HATNet survey observations, but was fully resolved by all subsequent follow-up observations. Figure 9 shows the $H$-band magnitude contrast curve for HAT-P-67 based on these observations. This curve was calculated using the method and software described by Espinoza et al. (2016). The band shown in this image represents the variation in the contrast limit depending on the position angle of the putative neighbor. We can rule out other neighbors with a magnitude difference of $\Delta H < 2$ mag, down to a separation of 0.″3; and $\Delta H < 6$ mag, down to a separation of 0.″8. The $L'$ observations suffered from high thermal background, and the 4.″9 neighbor was not detected. Based on these obversations, meaningful constraints could not be placed on closer neighbors in $L'$.

$J$-band snapshot images of HAT-P-67 were obtained with WHIRC on the night of 2016 April 24, with a seeing of ~0.″9. The images were collected at four nod positions, and were calibrated, background-subtracted, registered, and median-combined using the same tools that we used for reducing the KeplerCam images. The 4.″9 neighbor was not detected, and we concluded that it must have $\Delta J > 7$ mag. The closest neighbor detected in these observations was at a separation of 9.″3 to the northwest, and has a relative magnitude difference of $\Delta J = 4.96 \pm 0.01$ mag compared to HAT-P-67. Figure 9 shows the $J$-band magnitude contrast curve computed in a similar manner to the $H$-band contrast curve.

The DSSI observations were gathered between the nights of UT 2015 September 26 and UT 2015 October 3. A dichroic beamsplitter was used to obtain simultaneous imaging through 692 and 880 nm filters. Each observation consisted of a sequence of 1000 40 ms exposures read-out on 128 × 128 pixel (2.″8 × 2.″8) subframes, which were reduced to reconstructed images following Horch et al. (2011). These images were searched for companions, but none were detected. Based on this, the 5$\sigma$ lower limits on the differential magnitude between a putative companion and the primary star were determined as a function of angular separation as described in Horch et al. (2011). Based on these observations, we exclude neighbors with $\Delta m < 2.56$ at 692 nm or $\Delta m < 2.80$ at 880 nm down to a limiting separation of 0.″2 (see Figure 10).

### 3.8. Blend Analysis

Blend scenarios are eliminated by the detection of the planetary Doppler tomographic transit signal. Cases where an eclipsing binary blended with a foreground star iare the cause of the transit signal. In these cases, the Doppler tomographic shadow will be significantly diluted with respect to the photometric transit signal.

The flux under the shadow of the planet, as a fraction of the total flux under the rotational broadening kernel, describes the area blocked by the planet. This directly corresponds to a "transit light curve" over the broadband of the TRES spectrum (following Zhou et al. 2016a). We plot this Doppler tomographic light curve in Figure 4 (the bottom panel). We also plot the model transit light curve as per the global best-fit solution. The spectroscopic transit depth is consistent with that of the photometric transit depth, which confirms the lack of any significant dilution by background stars. The elimination of blend scenarios and the mass upper limit determined from HIRES radial velocities validates HAT-P-67b as a planet. We can also place strict upper limits on any third light contamination from background stars by modeling the line broadening profiles from the LSD analysis. A high signal-to-noise broadening profile was derived by averaging the 32 TRES spectra obtained for HAT-P-67. By modeling this profile as two stars, we place an upper limit on the flux ratio of any potential

[15] The WIYN Observatory is a joint facility of the University of Wisconsin-Madison, Indiana University, the National Optical Astronomy Observatory, and the University of Missouri.

**Table 5**
Stellar Parameters for HAT-P-67

| Parameter | Circular Fit Geneva | Eccentric Fit Geneva | Circular Fit Dartmouth | Eccentric Fit Dartmouth |
|---|---|---|---|---|
| Catalogue Information | | | | |
| Tycho-2 | 3084-533-1 | ⋯ | ⋯ | ⋯ |
| GSC | 03084-00533 | ⋯ | ⋯ | ⋯ |
| 2MASS | J17062656+4446371 | ⋯ | ⋯ | ⋯ |
| GAIA | 1358614978835493120 | ⋯ | ⋯ | ⋯ |
| GAIA RA (J2015) | 17:06:26.574 | ⋯ | ⋯ | ⋯ |
| GAIA DEC (J2015) | +44:46:36.794 | ⋯ | ⋯ | ⋯ |
| GAIA $\mu_\alpha$ (mas yr$^{-1}$) | 9.32 ± 0.88 | ⋯ | ⋯ | ⋯ |
| GAIA $\mu_\delta$ (mas yr$^{-1}$) | 18.5 ± 1.2 | ⋯ | ⋯ | ⋯ |
| GAIA Parallax[a] (mas) | 2.92 ± 0.23 | ⋯ | ⋯ | ⋯ |
| Spectroscopic properties[b c] | | | | |
| $T_{\rm eff\star}$(K) | $6406^{+65}_{-61}$ | $6408^{+63}_{-65}$ | $6406^{+58}_{-63}$ | $6414^{+69}_{-59}$ |
| [Fe/H] | −0.08 ± 0.05 | −0.08 ± 0.05 | $-0.07^{+0.04}_{-0.05}$ | −0.08 ± 0.05 |
| $v \sin I_\star$ (km s$^{-1}$) | 35.8 ± 1.1 | 35.8 ± 1.1 | $33.2^{+1.5}_{-1.2}$ | $33.9^{+1.2}_{-1.3}$ |
| Photometric properties | | | | |
| *GALEX*FUV (AB mag) | 19.759 ± 0.137 | ⋯ | ⋯ | ⋯ |
| *GALEX* NUV (AB mag) | 14.251 ± 0.007 | ⋯ | ⋯ | ⋯ |
| GAIA $g$ (mag) | 9.94 | ⋯ | ⋯ | ⋯ |
| APASS $B$ (mag) | 10.682 ± 0.010 | ⋯ | ⋯ | ⋯ |
| APASS $g'$ (mag) | 10.351 | ⋯ | ⋯ | ⋯ |
| APASS $V$ (mag) | 10.069 ± 0.016 | ⋯ | ⋯ | ⋯ |
| APASS $r'$ (mag) | 10.010 | ⋯ | ⋯ | ⋯ |
| TASS $I$ (mag) | 9.518 ± 0.048 | ⋯ | ⋯ | ⋯ |
| 2MASS $J$ (mag) | 9.145 ± 0.021 | ⋯ | ⋯ | ⋯ |
| 2MASS $H$ (mag) | 8.961 ± 0.019 | ⋯ | ⋯ | ⋯ |
| 2MASS $K_s$ (mag) | 8.900 ± 0.019 | ⋯ | ⋯ | ⋯ |
| Derived properties[b] | | | | |
| $M_\star(M_\odot)$ | $1.642^{+0.155}_{-0.072}$ | $1.73^{+0.21}_{-0.13}$ | 1.43 ± 0.05 | $1.38^{+0.05}_{-0.05}$ |
| $R_\star(R_\odot)$ | $2.546^{+0.099}_{-0.084}$ | $2.71^{+0.48}_{-0.39}$ | $2.389^{+0.040}_{-0.038}$ | $2.13^{+0.17}_{-0.14}$ |
| $\log g_\star$(cgs) | $3.854^{+0.014}_{-0.023}$ | $3.800^{+0.106}_{-0.080}$ | $3.837^{+0.009}_{-0.011}$ | $3.932^{+0.035}_{-0.060}$ |
| $L_\star(L_\odot)$ | $8.68^{+1.50}_{-0.86}$ | $8.3^{+4.0}_{-1.9}$ | $8.62^{+0.57}_{-0.50}$ | $6.8^{+1.2}_{-0.9}$ |
| $M_V$ (mag) | $2.50^{+0.13}_{-0.23}$ | $2.57^{+0.29}_{-0.37}$ | $2.403^{+0.083}_{-0.063}$ | $2.67^{+0.15}_{-0.17}$ |
| $M_K$ (mag,ESO) | $1.26^{+0.15}_{-0.34}$ | $1.36^{+0.25}_{-0.39}$ | $1.304^{+0.046}_{-0.045}$ | $1.56^{+0.14}_{-0.18}$ |
| $A_V$ (mag) | $<0.051(1\sigma)$ | $<0.061(1\sigma)$ | $<0.13(1\sigma)$ | $<0.11(1\sigma)$ |
| Age (Gyr) | $1.24^{+0.27}_{-0.22}$ | $1.00^{+0.21}_{-0.41}$ | $2.83^{+0.22}_{-0.19}$ | $3.04^{+0.31}_{-0.27}$ |
| Distance (pc) | $320^{+48}_{-14}$ | $322^{+35}_{-19}$ | $335^{+7}_{-7}$ | $297^{+26}_{-18}$ |

**Notes.**
[a] A correction of −0.325 ± 0.062 mas has been applied to the *GAIA* DR1 parallax, as per Stassun & Torres (2016).
[b] Derived from the global modeling described in Section 3.4, co-constrained by spectroscopic stellar parameters, and the *GAIA* parallax.
[c] These stellar parameters are heavily constrained by Gaussain priors around their derived values from the KECK-HIRES iodine-free spectrum using the SPC pipeline (Buchhave et al. 2012).

companion to be <0.004, or within 6 magnitudes of the primary star, with the caveat that any potential blended companion does not exhibit radial velocity variation.

## 4. Discussion

We presented the discovery of HAT-P-67b, a hot-Saturn transiting an F-subgiant. HAT-P-67b has a radius of $2.085^{+0.096}_{-0.071}\,R_{\rm J}$, and a mass constrained by radial velocity measurements to be $M_{\rm p} < 0.59\,M_{\rm J}$ at $1\sigma$. Confirmation of the planetary nature of HAT-P-67b involved numerous high precision follow-up transit light curves, radial velocity constraints on its mass, and two Doppler tomographic transits that eliminated potential blended eclipsing binary scenarios.

The mass, radius, and densities of HAT-P-67b are plotted in Figure 11, along with selected parts of the gas giant population. HAT-P-67b is one of the largest and one of the lowest density planets known ($\rho_p = 0.052^{+0.039}_{-0.028}$ g cm$^{-3}$). A number of other inflated gas giants have been discovered around subgiants (KOI-680b, Almenara et al. 2015; EPIC 206247743b, Van Eylen et al. 2016; KELT-8b, Fulton et al. 2015; KELT-11b, Pepper et al. 2016; and HAT-P-65b and HAT-P-66b, Hartman et al. 2016) and giants (e.g., EPIC 211351816b, Grunblatt et al. 2016). One hypothesis is that these gas giants are reinflated by the evolved host star (Lopez & Fortney 2016). In this scenario, as the host star evolves off the main sequence, "warm-Jupiters" are subjected to higher incident flux and stronger tidal heating (assuming a nonzero initial eccentricity). The heating reaches deep enough into the planetary interior to inflate the planet radius. Hartman et al. (2016) found empirical evidence that the level of planet inflation is correlated to the fractional age of the host star, which further supports the idea of reinflation. Figure 12 shows the evolution in the incident flux received

**Table 6**
Orbital and Planetary Parameters

| Parameter | Circular Fit Geneva | Eccentric Fit Geneva | Circular Fit Dartmouth | Eccentric Fit Dartmouth |
|---|---|---|---|---|
| Light curve parameters | | | | |
| $P$ (days) | $4.8101025^{+0.00000043}_{-0.00000033}$ | $4.8101038^{+0.00000054}_{-0.00000037}$ | $4.8101017^{+0.00000034}_{-0.00000030}$ | $4.8101082^{+0.00000052}_{-0.00000051}$ |
| $T_c$ (BJD)[a] | $2455961.38467^{+0.00076}_{-0.00064}$ | $2455961.38472^{+0.00090}_{-0.00082}$ | $2455961.38465^{+0.00074}_{-0.00065}$ | $2455961.3852^{+0.0008}_{-0.0010}$ |
| $T_{14}$ (days)[a] | $0.2912 \pm 0.0019$ | $0.308^{+0.029}_{-0.031}$ | $0.2910 \pm 0.0015$ | $0.257^{+0.019}_{-0.010}$ |
| $T_{12} = T_{34}$ (days)[a] | $0.0229 \pm 0.0010$ | $0.0246 \pm 0.0027$ | $0.02330^{+0.00030}_{-0.00055}$ | $0.0213^{+0.0015}_{-0.0014}$ |
| $a/R_\star$ | $5.691^{+0.057}_{-0.124}$ | $5.34^{+0.61}_{-0.46}$ | $5.659^{+0.066}_{-0.061}$ | $6.34^{+0.30}_{-0.42}$ |
| $R_p/R_\star$ | $0.0834 \pm 0.0017$ | $0.084^{+0.0019}_{-0.0020}$ | $0.0821^{+0.0013}_{-0.0009}$ | $0.0846^{+0.0016}_{-0.0018}$ |
| $b \equiv a \cos i/R_\star$ | $0.12^{+0.12}_{-0.08}$ | $0.12^{+0.12}_{-0.08}$ | $0.214^{+0.023}_{-0.045}$ | $0.20^{+0.11}_{-0.12}$ |
| $i$ (deg) | $88.8^{+1.1}_{-1.3}$ | $88.9 \pm 1.6$ | $88.37^{+0.61}_{-0.57}$ | $88.2^{+1.3}_{-1.1}$ |
| $\lvert\lambda\rvert$ (deg) | $2.9^{+6.4}_{-4.9}$ ($<14\ 1\sigma$) | $2.5^{+5.8}_{-4.6}$ ($<12\ 1\sigma$) | $-1.6^{+3.9}_{-4.6}$ ($<4\ 1\sigma$) | $2.3^{+6.6}_{-6.4}$ ($<13\ 1\sigma$) |
| Limb-darkening coefficients[b] | | | | |
| $a_r$ (linear term) | 0.2497 | ⋯ | ⋯ | ⋯ |
| $b_r$ (quadratic term) | 0.3765 | ⋯ | ⋯ | ⋯ |
| $a_I$ | 0.1701 | ⋯ | ⋯ | ⋯ |
| $b_I$ | 0.3744 | ⋯ | ⋯ | ⋯ |
| $a_i$ | 0.1897 | ⋯ | ⋯ | ⋯ |
| $b_i$ | 0.3747 | ⋯ | ⋯ | ⋯ |
| $a_z$ | 0.1397 | ⋯ | ⋯ | ⋯ |
| $b_z$ | 0.3661 | ⋯ | ⋯ | ⋯ |
| RV parameters | | | | |
| $K$ (m s$^{-1}$) | $<36(1\sigma)$ | $<52(1\sigma)$ | $<38(1\sigma)$ | $<37(1\sigma)$ |
| $e \cos \omega$ | | $-0.21^{+0.15}_{-0.14}$ | | $-0.03^{+0.20}_{-0.22}$ |
| $e \sin \omega$ | | $0.027^{+0.10}_{-0.11}$ | | $-0.150^{+0.075}_{-0.055}$ |
| $e$ | | $0.24 \pm 0.12$ | | $0.22^{+0.12}_{-0.08}$ |
| $\omega$ | | $172^{+31}_{-43}$ | | $105^{+46}_{-66}$ |
| RV jitter (m s$^{-1}$)[c] | 59 | 58 | 59 | 59 |
| Systemic RV (km s$^{-1}$)[d] | $-1.4 \pm 0.5$ | ⋯ | ⋯ | ⋯ |
| Planetary parameters | | | | |
| $M_p(M_J)$[e] | $0.34^{+0.25}_{-0.19}$ | $0.49^{+0.27}_{-0.22}$ | $0.33^{+0.22}_{-0.17}$ | $0.29^{+0.24}_{-0.19}$ |
| $R_p(R_J)$ | $2.085^{+0.096}_{-0.071}$ | $2.25^{+0.20}_{-0.23}$ | $1.975^{+0.045}_{-0.038}$ | $1.78^{+0.14}_{-0.10}$ |
| $\rho_p$(g cm$^{-3}$) | $0.052^{+0.039}_{-0.028}$ | $0.058^{+0.039}_{-0.025}$ | $0.058^{+0.039}_{-0.030}$ | $0.065^{+0.062}_{-0.044}$ |
| $\log g_p$ (cgs) | $2.32^{+0.24}_{-0.34}$ | $2.41^{+0.20}_{-0.25}$ | $3.837^{+0.009}_{-0.011}$ | $2.36^{+0.28}_{-0.47}$ |
| $a$ (au) | $0.06505^{+0.00273}_{-0.00079}$ | $0.0663^{+0.0016}_{-0.0014}$ | $0.062844^{+0.00053}_{-0.00049}$ | $0.061994^{+0.00068}_{-0.00072}$ |
| $T_{eq}$ (K) | $1903 \pm 25$ | $1963^{+85}_{-99}$ | $1903^{+19}_{-21}$ | $1803^{+62}_{-43}$ |
| $\Theta$[f] | $0.0138^{+0.0099}_{-0.0075}$ | $0.0178^{+0.0098}_{-0.0077}$ | $0.015^{+0.025}_{-0.015}$ | $0.015^{+0.013}_{-0.010}$ |
| $\langle F \rangle$ ($10^9$ erg s$^{-1}$ cm$^{-2}$)[g] | $2.74^{+0.19}_{-0.17}$ | $2.57^{+0.45}_{-0.46}$ | $2.98^{+0.14}_{-0.13}$ | $2.41^{+0.33}_{-0.25}$ |

**Notes.**
[a] $T_c$: reference epoch of mid-transit that minimizes the correlation with the orbital period. BJD is calculated from UTC. $T_{14}$: total transit duration, and time between first to last contact. $T_{12} = T_{34}$: ingress/egress time, and time between first and second, or third and fourth contact.
[b] Values for a quadratic law given separately for each of the filters with which photometric observations were obtained. These values were adopted from the tabulations by Claret & Bloemen (2011) according to the spectroscopic (SPC) parameters listed in Table 5. The limb darkening coefficients are held as fixed during the global modeling.
[c] This jitter was added linearly to the RV uncertainties for each instrument such that $\chi^2/\mathrm{dof} = 1$ for the observations from that instrument.
[d] The systemic RV for the system as measured relative to the telluric lines.
[e] The mass measurement is quoted as the median of the posterior, with the uncertainties defined as the 68 percentile region.
[f] The Safronov number is given by $\Theta = \frac{1}{2}(V_{esc}/V_{orb})^2 = (a/R_p)(M_p/M_\star)$ (see Hansen & Barman 2007).
[g] Incoming flux per unit surface area, which is averaged over the orbit.

by HAT-P-67b over its lifetime. Currently, HAT-P-67b receives ∼2× the incident flux of a zero-age main-sequence HAT-P-67, which is potentially inducing an inflation of the planetary radius.

Figure 12 also plots the incident flux received by the hot-Jupiter distribution against their planet masses. There is a paucity of low mass planets that receive high incident flux (a sharp envelope that likely resulted from the evaporation of Saturn and Neptune mass planets in close-in orbits (e.g., Lecavelier Des Etangs 2007; Ehrenreich & Désert 2011; Owen & Wu 2013)). HAT-P-67b lies on the edge of the envelope; unlike planets of similar masses that receive high incident irradiation, HAT-P-67b did not "boil-off," but survived through to present day. The high incident flux may also have halted contraction early on, which would lead to its current radius. Since there is a lack of inflated Saturn-mass planets in high incident flux environments, HAT-P-67b is an important point in the mass–radius-flux relationship.

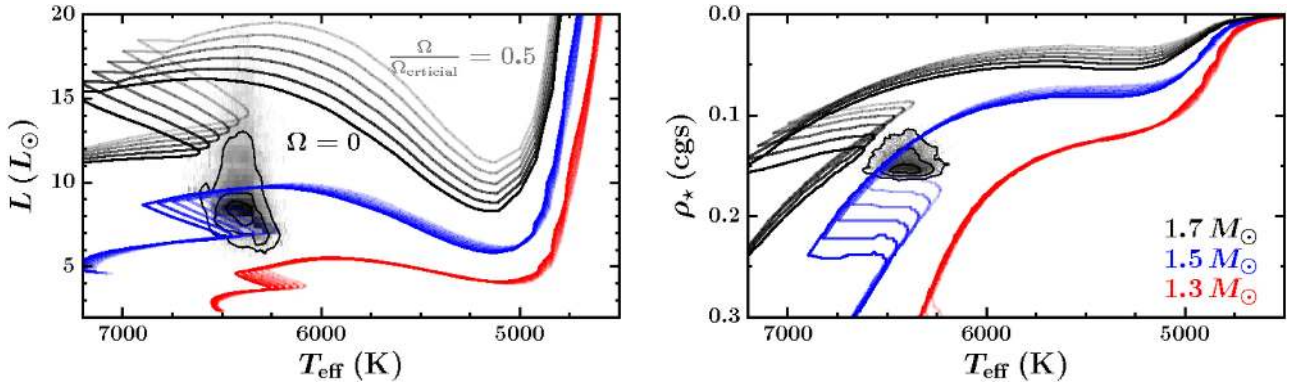


**Figure 6.** Model evolutionary tracks of effective temperature–luminosity (left) and effective temperature–stellar density (right) from the Geneva isochrones (Ekström et al. 2012) are plotted for solar metallicity stars of various masses and rotation rates. Red tracks denote stars of 1.3 $M_\odot$, blue for 1.5 $M_\odot$, and black for 1.7 $M_\odot$. The shades of the lines illustrate the influence of rotation on evolution, with darkest for no rotation, and lightest for $\Omega/\Omega_{\rm critical} = 0.5$ at 0.1 intervals. The 1, 2, and 3$\sigma$ contours for the posterior probability distribution of HAT-P-67 are plotted. Note that the effective temperature–stellar density distribution (right) is model independent, with effective temperature measured from spectra and stellar density derived from the transit duration. The effective temperature–luminosity distribution (left) requires isochrone interpolation of luminosity and is therefore model dependent.

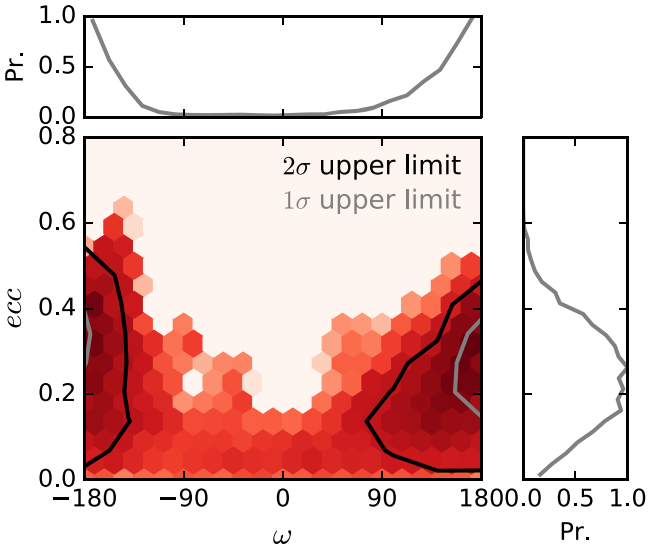


**Figure 7.** Eccentricity of HAT-P-67b is largely determined by the transit duration and the stellar radius derived from the light curves and *GAIA* distance. The eccentricity *ecc* and argument of periastron $\omega$ posteriors are plotted. The 64 and 95 percentile contours are plotted in gray and black, respectively.

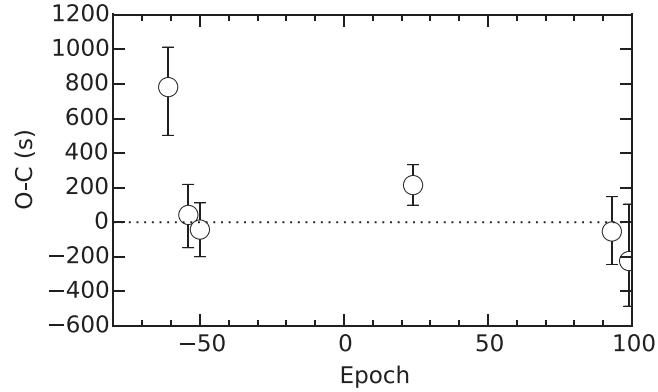


**Figure 8.** Transit centroid offsets (*O*–*C*) for the follow-up light curves. We do not find convincing evidence for transiting timing variations that may be indicative of additional orbiting companions.

The low density and high irradiation of HAT-P-67b also results in a bloated atmosphere, with a large scale height of ∼500 km (assuming an $H_2$ atmosphere), which makes the planet a good candidate for transmission spectroscopy follow-up studies.

In addition, X-ray- and EUV-driven hydrodynamic escape plays an especially important role in low density, low mass planets (e.g., Lecavelier Des Etangs 2007; Murray-Clay et al. 2009; Ehrenreich & Désert 2011; Owen & Jackson 2012; Owen & Wu 2013). For hot-Jupiters, X-ray and EUV photoionizes the upper atmosphere, therefore causing it to heat up and expand, which results in escaping flows. Atmospheric escape has been observed for HD 209458 b (Vidal-Madjar et al. 2003, 2004) and HD 189733 b (Lecavelier Des Etangs et al. 2010), where the Ly$\alpha$ radii of the planets are ∼10 times larger than their optical radii and extend beyond the Roche sphere. Since the mass loss rate is largely proportional to the incident UV and X-ray flux received by the planets (e.g., Murray-Clay et al. 2009), we checked for existing X-ray and UV measurements of HAT-P-67. While EUV or X-ray flux measurements do not exist, HAT-P-67 is identified as a source by *GALEX*, with flux measurements in the FUV (1344–1786 Å) and NUV (1771–2831 Å) bands. In Figure 13, we compile all transiting planet systems with *GALEX* FUV and NUV measurements (Bianchi et al. 2011), as well as *GAIA* parallaxes and updated system parameters from Stassun et al. (2016). To examine the potential mass loss rate of HAT-P-67b in the context of existing systems, we plot the UV fluxes received by each planet (normalized to that received by HD 209458 b) against their escape velocities. HAT-P-67b receives 24 times the FUV and 10 times the NUV flux of HD 209458 b, and has one of the lowest escape velocities of known transiting planets (25 km s$^{-1}$, compared to 43 km s$^{-1}$ for HD 209458 b). As such, it should be an excellent target for Ly$\alpha$ transit observations to measure its extended hydrogen exosphere.

HAT-P-67 has the highest $v \sin I_\star$ among all the evolved planet hosts (35.8 ± 1.1 km s$^{-1}$), which allows us to spectroscopically measure its projected spin alignment angle. The only previous Holt–Rossiter–McLaughlin measurement of a planet around a subgiant was WASP-71b (Smith et al. 2013), which was found to be in a well-aligned orbit. Two additional planet-hosting evolved stars have had their line-of-sight stellar inclination measured via asteroseismology. Quinn et al. (2015) found the super-Jupiter Kepler-432b to be spin–orbit aligned in a eccentric, with a 53 day period orbit around a red-

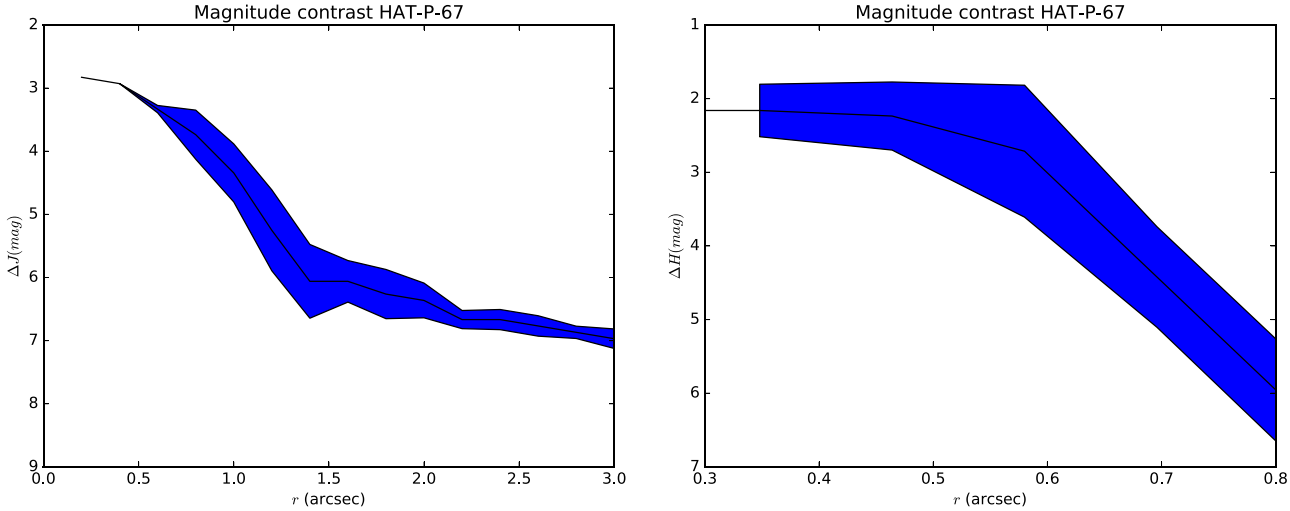


**Figure 9.** Contrast curve for HAT-P-67 in the (left) *J*-band based on observations made with WHIRC on the WIYN 3.5 m and (right) the *H*-band based on Clio2/MMT observations as described in Section 3.7. The bands show the variation in the contrast limits depending on the position angle of the putative neighbor.

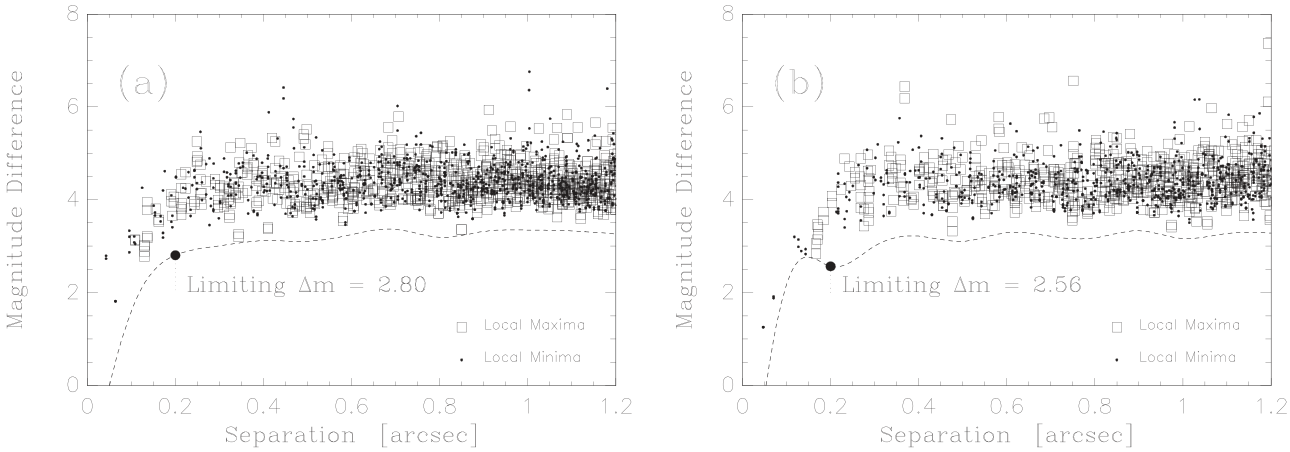


**Figure 10.** Limits on the relative magnitude of a resolved companion to HAT-P-67 as a function of angular separation based on speckle imaging observations from WIYN 3.5 m/DSSI. The dotted lines denote the $5\sigma$ limits. The left panel shows the limits for the 692 nm filter, and the right shows limits for the 880 nm filter.

giant. Huber et al. (2013) found two co-planar planets residing in inclined orbits around their red-giant host Kepler-56.

As a host star expands over its post main-sequence evolution, star–planet tidal interaction should increase in strength, which then modifies the orbit of the planet. Radial velocity searches have found that eccentric planets are rarer around evolved hosts than around dwarfs (e.g., Jones et al. 2014). However, tidal interactions are likely weak during the lifetime of HAT-P-67b; the characteristic timescale for orbital decay is on the order of $\sim 10^{11}$ years (adopting Equation (2) of Hansen 2012 and assumes an effective stellar dissipation coefficient of $\sigma_\star = 10^{-8}$). Similarly, the tidal synchronization timescale—the time taken to synchronize the stellar spin vector with the orbit normal vector, leading to spin–orbit alignment and spin–orbit synchronization— is $\sim 10^{13}$ yr (Equation (3) of Hansen 2012), so the stellar spin is unlikely to have been modified over the lifetime of the system due to planet–star tidal interactions. The same cannot be said of WASP-71b, which orbits at a shorter period of 2.9 days, and has a characteristic synchronization timescale of $\sim 10^{10}$ yr, which is short enough that tides likely played a role in modifying the spin of the host star.

HAT-P-67b is part of a growing list of planets confirmed via Doppler tomography, which includes WASP-33b (Collier Cameron et al. 2010b; Johnson et al. 2015), Kepler-13b (Johnson et al. 2014), KELT-7b (Bieryla et al. 2015; Zhou et al. 2016a), HAT-P-57b (Hartman et al. 2015), KOI-12b (Bourrier et al. 2015), KELT-17b (Zhou et al. 2016b), and XO-6b (Crouzet et al. 2016). The routine success of the Doppler tomography technique yields exciting prospects to fill the paucity of transiting planets around early-type stars.

We thank the referee for their insightful contributions to this manuscript. HATNet operations have been funded by NASA grants NNG04GN74G and NNX13AJ15G. The follow-up of HATNet targets has been partially supported through NSF grant AST-1108686. G.Á.B., Z.C., and K.P. acknowledge partial support from NASA grant NNX09AB29G. J.H. acknowledges support from NASA grant NNX14AE87G. K. P. acknowledges support from NASA grant NNX13AQ62G. We acknowledge partial support also from the *Kepler* Mission under NASA Cooperative Agreement NCC2-1390 (DWL, PI). Data presented in this paper are based on observations obtained at the HAT station at the Submillimeter Array of SAO and the

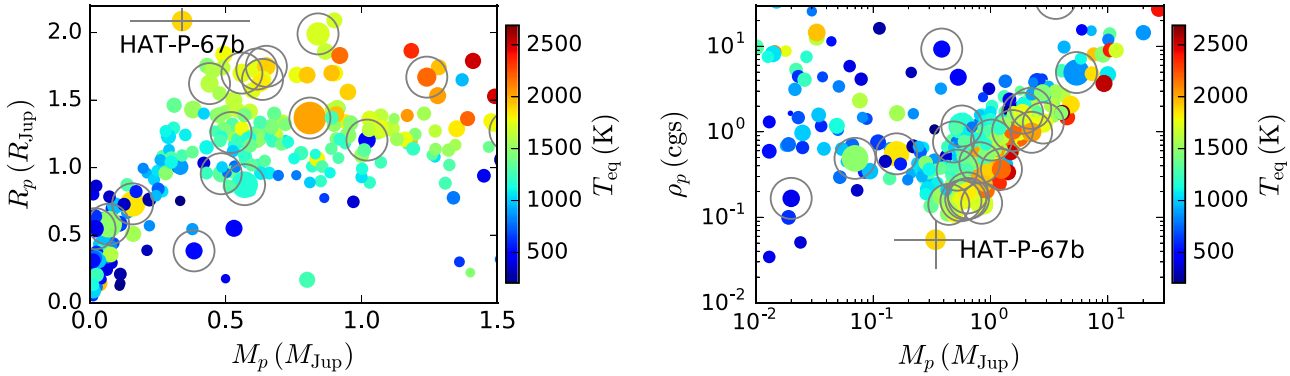


**Figure 11.** Mass–radius and mass–density distributions of known transiting exoplanets are plotted. The colors of the points represent the equilibrium temperatures of the planets, while their sizes are scaled to indicate the radii of the host stars. Planets that orbit evolved stars ($\log g < 4.0$) are marked by the open gray circles. HAT-P-67b is labeled, and its $1\sigma$ uncertainties are shown by the error bars. We note that it is one of the largest radius and lowest density planets found to date.

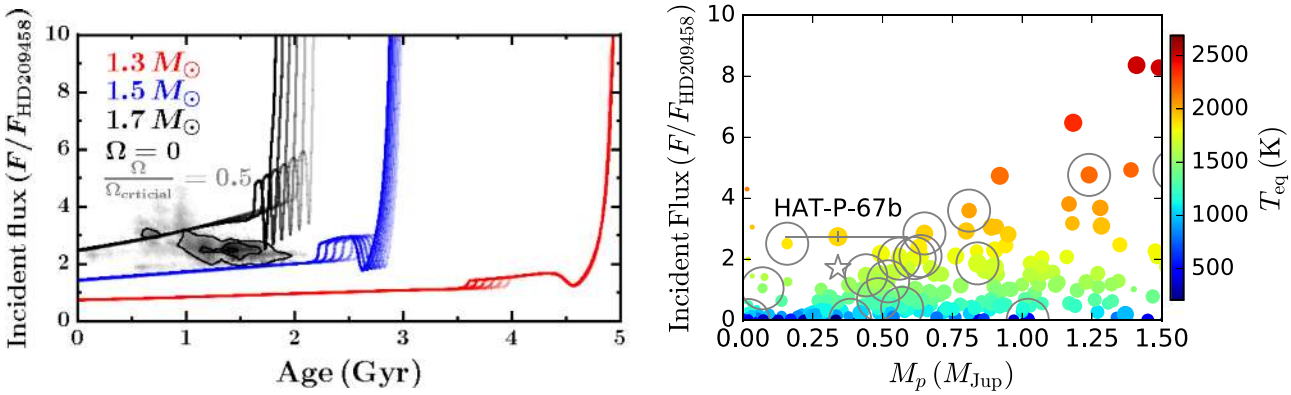


**Figure 12.** Incident flux received by HAT-P-67b. The left panel shows the changing incident flux of HAT-P-67b, which was calculated from the adopted Geneva isochrones. The line color and shading correspond with that shown in Figure 6. The right panel shows the distribution of incident flux received by the transiting planet distribution, as a function of planet mass. The colors of individual points indicate their equilibrium temperatures, while the size of the points are scaled to the radii of the planets. The Zero Age Main Sequence (ZAMS) incident flux of HAT-P-67b is marked by the gray star. Planets that orbit evolved stars ($\log g < 4.0$) are marked by open gray circles.

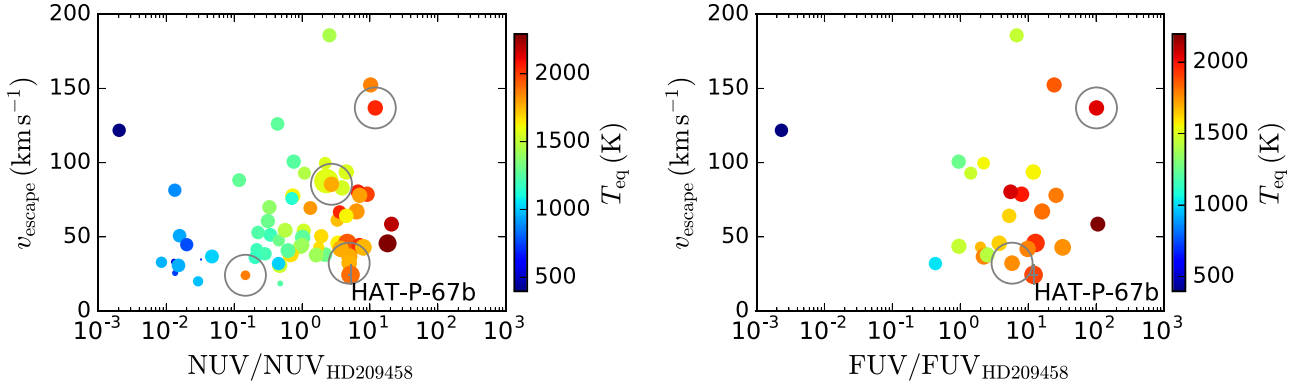


**Figure 13.** Mass loss is driven by UV and X-ray irradiation of the upper atmosphere of planets. HAT-P-67b potentially has one of the highest mass loss rates of known hot-Jupiters. We plot the NUV left and FUV right fluxes received by known transiting systems against their escape velocities. Only systems with *GALEX* UV fluxes (Bianchi et al. 2011) and *GAIA* parallaxes are plotted. As in Figure 11, the sizes of the points indicate their planetary radii, while the colors represent the equilibrium temperatures. Planets orbiting evolved stars are marked by open gray circles.

HAT station at the Fred Lawrence Whipple Observatory of SAO. This research has made use of the NASA Exoplanet Archive, which is operated by the California Institute of Technology, under contract with the National Aeronautics and Space Administration under the Exoplanet Exploration Program. Data presented herein were obtained at the WIYN Observatory from telescope time allocated to NN-EXPLORE through the scientific partnership of the National Aeronautics and Space Administration, the National Science Foundation, and the National Optical Astronomy Observatory. This work was supported by a NASA WIYN PI Data Award, administered by the NASA Exoplanet Science Institute. We acknowledge of J.A. Johnson in supporting the KECK-HIRES observations. The authors wish to recognize and acknowledge the very

significant cultural role and reverence that the summit of Mauna Kea has always had within the indigenous Hawaiian community. We are most fortunate to have the opportunity to conduct observations from this mountain.

## References


Almenara, J. M., Damiani, C., Bouchy, F., et al. 2015, A&A, 575, A71
Bakos, G., Noyes, R. W., Kovács, G., et al. 2004, PASP, 116, 266
Bakos, G. Á, Kovács, G., Torres, G., et al. 2007, ApJ, 670, 826
Bakos, G. Á, Torres, G., Pál, A., et al. 2010, ApJ, 710, 1724
Béky, B., Bakos, G. Á, Hartman, J., et al. 2011, ApJ, 734, 109
Bianchi, L., Herald, J., Efremova, B., et al. 2011, Ap&SS, 335, 161
Bieryla, A., Collins, K., Beatty, T. G., et al. 2015, AJ, 150, 12
Bourrier, V., Lecavelier des Etangs, A., Hébrard, G., et al. 2015, A&A, 579, A55
Bowler, B. P., Johnson, J. A., Marcy, G. W., et al. 2010, ApJ, 709, 396
Buchhave, L. A., Bakos, G. Á, Hartman, J. D., et al. 2010, ApJ, 720, 1118
Buchhave, L. A., Latham, D. W., Johansen, A., et al. 2012, Natur, 486, 375
Butler, R. P., Marcy, G. W., Williams, E., et al. 1996, PASP, 108, 500
Casertano, S., Riess, A. G., Bucciarelli, B., & Lattanzi, M. G. 2016, arXiv:1609.05175
Castelli, F., & Kurucz, R. L. 2004, arXiv:astro-ph/0405087
Ciceri, S., Lillo-Box, J., Southworth, J., et al. 2015, A&A, 573, L5
Claret, A., & Bloemen, S. 2011, A&A, 529, A75
Collier Cameron, A., Bruce, V. A., Miller, G. R. M., Triaud, A. H. M. J., & Queloz, D. 2010a, MNRAS, 403, 151
Collier Cameron, A., Guenther, E., Smalley, B., et al. 2010b, MNRAS, 407, 507
Crouzet, N., McCullough, P. R., Long, D., et al. 2016, arXiv:1612.02776
Dawson, R. I., & Johnson, J. A. 2012, ApJ, 756, 122
Dobbs-Dixon, I., Lin, D. N. C., & Mardling, R. A. 2004, ApJ, 610, 464
Donati, J.-F., Semel, M., Carter, B. D., Rees, D. E., & Collier Cameron, A. 1997, MNRAS, 291, 658
Dotter, A., Chaboyer, B., Jevremović, D., et al. 2008, ApJS, 178, 89
Ehrenreich, D., & Désert, J.-M. 2011, A&A, 529, A136
Ekström, S., Georgy, C., Eggenberger, P., et al. 2012, A&A, 537, A146
Enoch, B., Collier Cameron, A., & Horne, K. 2012, A&A, 540, A99
Espinoza, N., Bayliss, D., Hartman, J. D., et al. 2016, AJ, 152, 108
Foreman-Mackey, D., Hogg, D. W., Lang, D., & Goodman, J. 2013, PASP, 125, 306
Freed, M., Hinz, P. M., Meyer, M. R., Milton, N. M., & Lloyd-Hart, M. 2004, Proc. SPIE, 5492, 1561
Fűrész, G. 2008, PhD thesis, Univ. Szeged
Fulton, B. J., Collins, K. A., Gaudi, B. S., et al. 2015, ApJ, 810, 30
Gray, R. O., & Corbally, C. J. 1994, AJ, 107, 742
Grunblatt, S. K., Huber, D., Gaidos, E. J., et al. 2016, arXiv:1606.05818
Hansen, B. M. S. 2012, ApJ, 757, 6
Hansen, B. M. S., & Barman, T. 2007, ApJ, 671, 861
Hartman, J. D., Bakos, G. Á, Bhatti, W., et al. 2016, arXiv:1609.02767
Hartman, J. D., Bakos, G. Á, Buchhave, L. A., et al. 2015, AJ, 150, 197
Hartman, J. D., Bakos, G. Á, Torres, G., et al. 2011, ApJ, 742, 59
Holt, J. R. 1893, AstAp, 12, 646
Horch, E. P., Bahi, L. A. P., Gaulin, J. R., et al. 2012, AJ, 143, 10
Horch, E. P., van Altena, W. F., Howell, S. B., Sherry, W. H., & Ciardi, D. R. 2011, AJ, 141, 180
Howell, S. B., Everett, M. E., Sherry, W., Horch, E., & Ciardi, D. R. 2011, AJ, 142, 19
Huber, D., Carter, J. A., Barbieri, M., et al. 2013, Sci, 342, 331
Jao, W.-C., Henry, T. J., Riedel, A. R., et al. 2016, ApJL, 832, L18
Johnson, J. A., Aller, K. M., Howard, A. W., & Crepp, J. R. 2010, PASP, 122, 905
Johnson, J. A., Butler, R. P., Marcy, G. W., et al. 2007, ApJ, 670, 833
Johnson, M. C., Cochran, W. D., Albrecht, S., et al. 2014, ApJ, 790, 30
Johnson, M. C., Cochran, W. D., Collier Cameron, A., & Bayliss, D. 2015, ApJL, 810, L23
Jones, M. I., Jenkins, J. S., Bluhm, P., Rojo, P., & Melo, C. H. F. 2014, A&A, 566, A113
Kipping, D. M. 2008, MNRAS, 389, 1383
Kipping, D. M. 2013, MNRAS, 434, L51
Kovács, G., Bakos, G., & Noyes, R. W. 2005, MNRAS, 356, 557
Kovács, G., Zucker, S., & Mazeh, T. 2002, A&A, 391, 369
Lecavelier Des Etangs, A. 2007, A&A, 461, 1185
Lecavelier Des Etangs, A., Ehrenreich, D., Vidal-Madjar, A., et al. 2010, A&A, 514, A72
Lecavelier des Etangs, A., Vidal-Madjar, A., McConnell, J. C., & Hébrard, G. 2004, A&A, 418, L1
Lillo-Box, J., Barrado, D., Moya, A., et al. 2014, A&A, 562, A109
Lindegren, L., Lammers, U., Bastian, U., et al. 2016, arXiv:1609.04303
Lopez, E. D., & Fortney, J. J. 2016, ApJ, 818, 4
Lovis, C., & Mayor, M. 2007, A&A, 472, 657
Mandel, K., & Agol, E. 2002, ApJL, 580, L171
McLaughlin, D. B. 1924, ApJ, 60, 22
Meynet, G., & Maeder, A. 2000, A&A, 361, 101
Murray-Clay, R. A., Chiang, E. I., & Murray, N. 2009, ApJ, 693, 23
Muzerolle, J., Hillenbrand, L., Calvet, N., Briceño, C., & Hartmann, L. 2003, ApJ, 592, 266
Natta, A., Testi, L., & Randich, S. 2006, A&A, 452, 245
Owen, J. E., & Jackson, A. P. 2012, MNRAS, 425, 2931
Owen, J. E., & Wu, Y. 2013, ApJ, 775, 105
Pepper, J., Rodriguez, J. E., Collins, K. A., et al. 2016, arXiv:1607.01755
Quinn, S. N., White, T. R., Latham, D. W., et al. 2015, ApJ, 803, 49
Rossiter, R. A. 1924, ApJ, 60, 15
Seager, S., & Mallén-Ornelas, G. 2003, in ASP Conf. Ser. 294, Scientific Frontiers in Research on Extrasolar Planets, ed. D. Deming & S. Seager (San Francisco, CA: ASP), 419
Shporer, A., Jenkins, J. M., Rowe, J. F., et al. 2011, AJ, 142, 195
Silva Aguirre, V., Lund, M. N., Antia, H. M., et al. 2016, arXiv:1611.08776
Skrutskie, M. F., Cutri, R. M., Stiening, R., et al. 2006, AJ, 131, 1163
Smith, A. M. S., Anderson, D. R., Bouchy, F., et al. 2013, A&A, 552, A120
Sozzetti, A., Torres, G., Charbonneau, D., et al. 2007, ApJ, 664, 1190
Stassun, K. G., Collins, K. A., & Gaudi, B. S. 2016, arXiv:1609.04389
Stassun, K. G., & Torres, G. 2016, ApJL, 831, L6
Szabó, G. M., Szabó, R., Benkő, J. M., et al. 2011, ApJL, 736, L4
Telting, J. H., Avila, G., Buchhave, L., et al. 2014, AN, 335, 41
Torres, G., Bakos, G. Á., Kovács, G., et al. 2007, ApJL, 666, L121
Van Eylen, V., Albrecht, S., Gandolfi, D., et al. 2016, AJ, 152, 143
Vidal-Madjar, A., Désert, J.-M., Lecavelier des Etangs, A., et al. 2004, ApJL, 604, L69
Vidal-Madjar, A., Lecavelier des Etangs, A., Désert, J.-M., et al. 2003, Natur, 422, 143
Vogt, S. S., Allen, S. L., Bigelow, B. C., et al. 1994, Proc. SPIE, 2198, 362
Wittenmyer, R. A., Endl, M., Wang, L., et al. 2011, ApJ, 743, 184
Zhou, G., Latham, D. W., Bieryla, A., et al. 2016a, MNRAS, 460, 3376
Zhou, G., Rodriguez, J. E., Collins, K. A., et al. 2016b, AJ, 152, 136